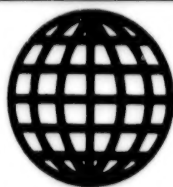**FOREIGN
BROADCAST
INFORMATION
SERVICE**

JPRS Report

Science &
Technology

China

SCIENCE & TECHNOLOGY

CHINA

CONTENTS

Experimental Research in Soft X-Ray Laser Gain

[Article by Xu Zhizhan [1776 5267 1455], Zhang Zhengquan [1728 2973 3123], Fan Pingzhong [5400 0756 1813], Chen Shisheng [7115 2514 0524], Lin Lihuang [2651 4409 3553], Lu Peixiang [7120 1014 4382], Wang Xiaofang [3769 2556 2455], Qian Aidi [6929 1947 1229], Yu Jiajin [0151 0502 6651], and Feng Xianping [7458 6343 1627] of Shanghai Institute of Optics and Fine Mechanics, Chinese Academy of Sciences, Shanghai 201800: "Experimental Research in Soft-X-Ray Laser Gain," a major Chinese Academy of Sciences project supported by the Chinese National Natural Science Foundation and the Chinese National High-Tech Program; See also earlier report in JPRS-CST-90-009, 6 Apr 90, pp 11-12]

[Text] Abstract

Combination-pumped soft X-ray laser gain experiments have been successfully carried out using the six-path laser facility and the LF12 laser facility at Shanghai Institute of Optics and Fine Mechanics (SIOFM). The amplified spontaneous emission (ASE) characteristics of Li-like Al and Si ions in a linear plasma produced by irradiating a target with a linearly focused laser were investigated. An independently developed grazing-incidence-grating spectrograph (GIGS) with one-dimensional spatial resolution and a pinhole transmission grating spectrograph (PTGS) were used to determine the axial time-integrated intensities of the emission lines of lithium-like aluminum and silicon ions from linear plasma of various lengths. It was found that the spectral line intensities corresponding to the 5f-3d transition of the Al^{10+} ion (wavelength 105.7 Å) and the 5f-3d transition (wavelength 88.9 Å) and 5d-3p transition (wavelength 87.3 Å) of the Si^{11+} ion increase non-linearly with the length of the plasma. The gain factors are 3.1 ± 0.9, 1.5 ± 0.5, and 1.4 ± 0.5 cm^{-1}, respectively. The maximum gain length product is approximately 2.5.

This is the first time that the 5f-3d and 5d-3p transitions of the Li-like Si^{11+} ion have been observed experimentally. The soft X-ray laser wavelength is under 100 Å. It is especially significant that the

results were obtained under a low pumping laser power density. Other research shows that with the Li-like combination mechanism it is feasible to push the soft X-ray laser to the "water window" band (43.8 - 23.3 Å) with our existing laser facility.

Key Words: Soft X-Ray Laser, Laser Gain

I. Introduction

Since the successful demonstration of using a laser-induced plasma as the gain medium for the ASE of soft X-rays[1, 2], many beneficial attempts have been made to improve the characteristics of the X-ray laser[3-7], particularly with regard to shorter wavelengths and higher efficiency. There are two major pumping mechanisms for the X-ray laser: electron collision excitation and three-body combination pumping. As far as the electron collision excitation mechanism is concerned, a high gain requires high plasma temperature and high plasma density (500-1000 eV, $10^{20}-10^{21}/cm^3$). In order to obtain short wavelengths, it is necessary to produce highly ionized ions of elements with a large Z number. Therefore, most experiments can only be done at some large laser facilities. The three-body combination pumping mechanism has lower plasma requirements (10-50 eV, $10^{19}/cm^3$). It uses the rapid cooling combination of hydrogen-like, lithium-like or sodium-like ions in a plasma of elements of medium Z number to greatly improve the efficiency of the soft X-ray laser. Therefore, the requirement for the driving laser is lower than that for electron collision excitation. Regardless of the pumping mechanism, no one has grasped the optimum experimental conditions. A variety of targets, such as fine fiber, thin foil, plate and magnetically confined laser plasma, has been used in combination pumping experiments. In electron collision excitation pumping experiments, foil, plate and other structurally complicated targets have been used. Fine fiber target, in spite of very rapid adiabatic expansion and cooling, has very poor laser coupling efficiency. Foil and plate have a higher coupling efficiency to effectively utilize the pumping power. This is particularly important to experiments done with a small laser. As far as understanding the fluid dynamic conditions to improve and optimize the laser output, there is a need to investigate the matter in detail for various targets and major pumping schemes.

The combination pumping of Li-like ions is an important three-body pumping scheme for obtaining soft X-ray lasing. Its requirement on the driving laser (linearly focused laser intensity generally in the range of $10^{12}-10^{13}$ W/cm^2) is not only lower than that for electron collision excitation but also much lower than that for pumping hydrogen-like ions. In addition, the pulse width and wavelength requirements are also not very strict. Furthermore, the technique approaches short wavelengths faster than Z^{-2}. Hence, it is more feasible to demonstrate the ASE

effect with a small driving laser using the Li-like ion combination pumping mechanism. With a large high-power laser, it would be possible to achieve a high gain-length product and obtain lasing at a wavelength shorter than that of the "water window" (23.3-43.8 Å).

Research on the soft X-ray laser involving Li-like Al^{10+} ions began at the South Paris University in France[7]. Most of their experiments were done with a 1.06-μm neodymium-glass laser with a pulse width ranging from 1 to several dozen nanoseconds. Absorption spectroscopy was successfully used to demonstrate the ASE effect of the 5f-3d transition of Mg^{9+} and Al^{10+} at 127.9 and 105.7 Å, respectively. In addition, preliminary measurements were made to determine the gain of the 5f-3d transition of S^{13+} at 65.2 Å[8]. The amplification of the 5f-3d and 5d-3p (103.8 Å) transitions or 4f-3d transition (154.7 Å) of Al^{10+} has been studied at Osaka University in Japan and Rutherford Laboratory in England[4,9] using a frequency-doubled neodymium-glass pulsed laser. The Institute of Physical Chemistry in Japan achieved the amplification of the 5f-3d and 4f-3d transitions of Al^{10+} with a smaller laser[10]. The laser amplification of the Al^{10+} 4f-3d transition and Si^{11+} 4f-3d transition (129 Å) was obtained at the Plasma Physics Laboratory at Princeton University using a high-power CO_2 laser and a strong magnetic field[11]. Up to now, no report has been found concerning the laser amplification of the 5f-3d (88.9 Å) and 5d-3p (87.3 Å) transitions involving Si^{11+}.

Based on the above considerations, soft X-ray gain experiments were done on the sixth-path neodymium-glass laser facility[12] and the LF12 laser facility[13] at SIOFM by irradiating aluminum and silicon plates with a line of focused laser beams and then measuring the effect using an independently developed GIGS with one-dimensional spatial resolution. Significant amplification of soft X-rays corresponding to the combination pumping of Li-like ions such as the 5f-3d transition of Al^{10+} (105.7 Å) and the 5f-3d transition (88.9 Å) and 5d-3p transition (87.3 Å) of Si^{11+} was experimentally confirmed.

II. Experimental Setup

The experiments involving Li-like Al^{10+} ions were carried out on the six-path laser shown schematically in Figure 1. In the experiment, two of the six laser beams were combined into one. The 1.06-μm laser beam used to irradiate the target consists of two pulses: each pulse is 250-300 ps wide and the two peaks are approximately 200 ps apart. The total energy of this combined laser pulse is about 15 J [joules] with a fluctuation of ±25 percent and a pulse width of 500 ps. The laser beam was focused on the target plate by a combination of cylindrical and a spherical lens to produce a line of highly ionized laser plasma which acts as the gain medium for the X-ray laser. The focal line is 10 mm long and approximately 200 μm wide, corresponding to a mean laser intensity of 1.5×10^{12} W/cm^2 on the target surface. Flat strips 1 mm thick were used as targets. In previous experiments[14], we observed

a large-scale plasma flow at the boundary between the hot plasma and cold target. In order to avoid this edge effect and to ensure the uniform irradiation at the center of the focal line, the width of the target plate must be less than the length of the focal line.
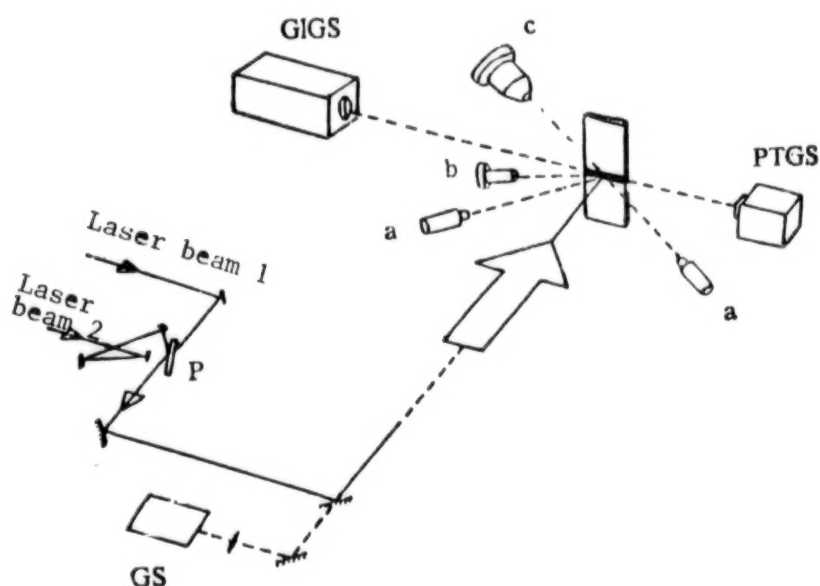

Figure 1. Experimental Setup

(GIGS - grazing incidence grating spectrograph, PTGS - pinhole transmission grating spectrograph, GS - grating spectrograph, a - Faraday cup, b - X-ray pinhole camera, c - T1AP flat crystal X-ray spectrograph, P- polarizer)

The primary diagnostic devices used in these experiments include an independently developed and constructed stigmatic GIGS with one-dimensional spatial resolution [15] and a PTGS [16]. These two spectrographs were aligned on the two ends of the focal line. In addition, a T1AP flat crystal spectrograph was placed on the side to photograph the space-resolved X-ray spectrum over time in order to monitor the resonance lines of higher-order ions between 6 and 14 Å. The X-ray emission image of the plasma was taken with a pinhole X-ray camera. A Faraday-cup charge collector was used to detect the ionic emission characteristics of the plasma. In addition, a one-dimensional-resolution grating spectrograph was used to measure the back-scattered second-order harmonics.

The 1-m XUV [extreme ultraviolet] GIGS is equipped with a 2400 lines/mm, 2°-glittering-angle gold-plated grating. The spectrum range is 20-120 Å. When the incident slit width is 5 μm, the resolution of the spectrum is 0.05 Å (as shown in Figure 2). The soft X-ray spectrum was recorded on Shanghai 5F medical X-ray film without a protective layer.
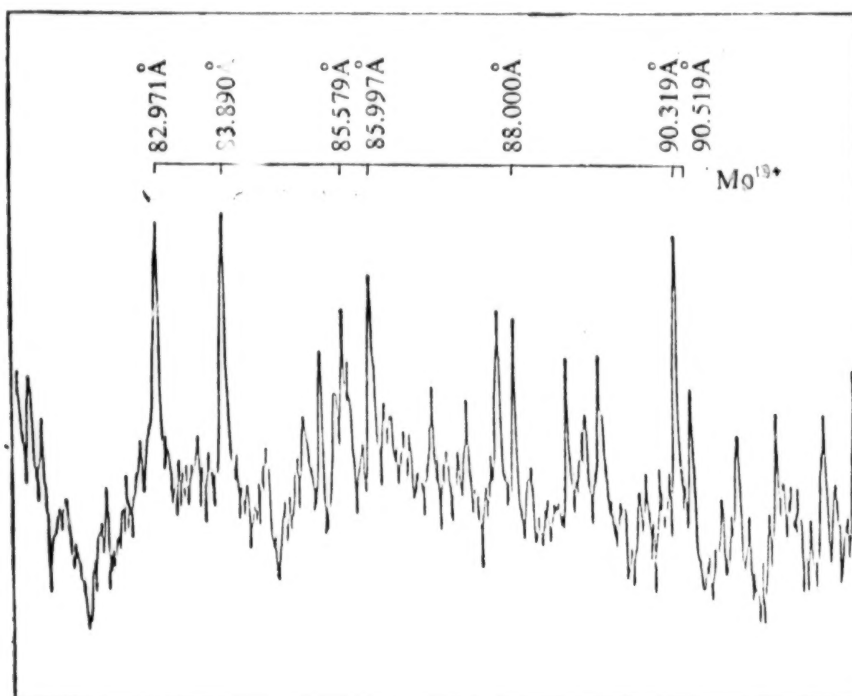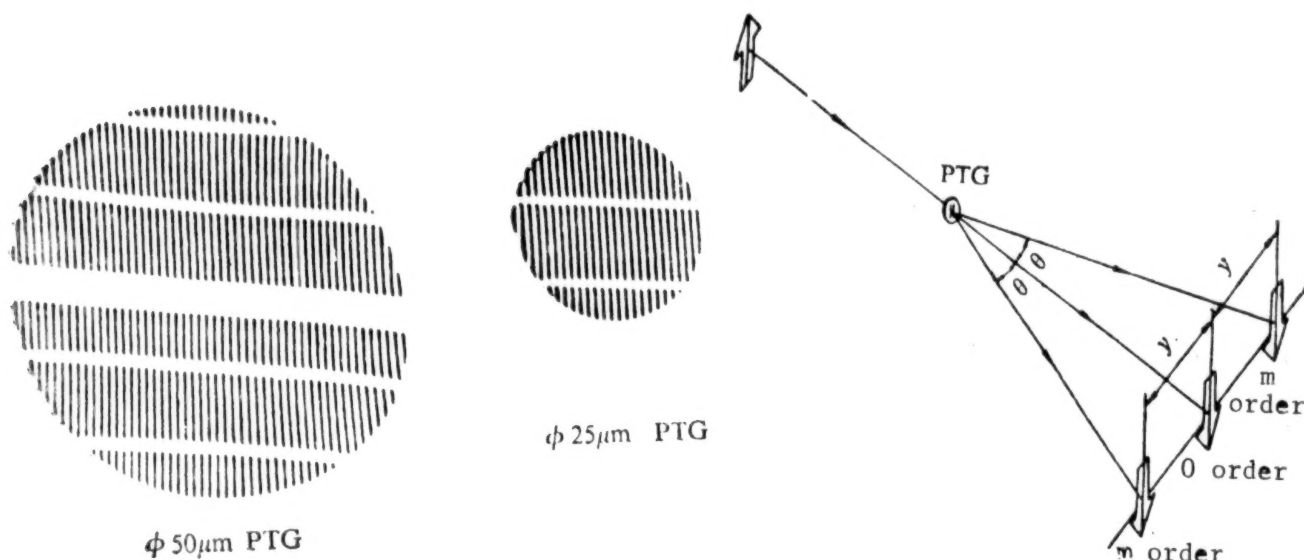

Figure 2. XUV Spectrum of Molybdenum Plasma Using a GIGS (5-μm Slit) (Spectral resolution of 0.05 Å was demonstrated)

The image of the plasma X-ray source with one-dimensional spatial resolution could be obtained using a GIGS with a grazing-incidence hypertorus mirror. The slit of the spectrograph is parallel to the optical axis of the driving laser, i.e., normal to the target surface. The two radii of curvature of the gold-plated hypertorus mirror are 3315 mm and 30.5 mm, respectively. Two astigmatic images of the laser plasma were formed, one at the incident slit of the grating spectrograph and the other at the diffracted image produced by the spherical grating at wavelength λ. Thus, a one-dimensional image of the laser plasma was found on the film at wavelength λ perpendicular to the target surface (as shown in Figure 3(a) [photograph not reproduced]). Figure 3(b) shows that the instrument has a spatial resolution of 50 μm. The distance between the hypertorus mirror and the X-ray source could be adjusted. In this work, however, it was fixed at 55 cm. The spatial amplification of the instrument was approximately 1. The optical axis of the spectrograph could be aligned with the axis of the focal line using the hypertorus mirror at an accuracy of 0.1 mrad [milliradian] and 50 μm. The angular accuracy of line focusing is approximately ± 2 mrad and the collective optical angle of the hypertorus mirror is 5-10 mrad.

Opposite to the GIGS, a PTGS was placed on the other end of the focal line (as shown in Figure 4). The aperture of the pinhole was either 25 μm or 50 μm, and the spectral range was 5-200 Å. The grating has either 1000 or 2000 lines per mm.

φ 50μm PTG

φ 25μm PTG

(a) Scanning Electron Micrographs of 25-μm and 50-μm-diameter PTG at 900 X (grating lines 1 μm apart)

(b) PTG Diffraction Image-Forming Principle (spectral resolution: 1000 lines/mm, $\Lambda\lambda s \sim 4$ Å; 2000 lines/mm, $\Lambda\lambda s \sim 2$ Å)

Figure 4. PTG (pinhole transmission grating) ((a) pictures and (b) principle of diffraction image formation)

Because the energy of the driving laser is low, the intensity of the converted soft X-ray is also low. Therefore, the spectrum was taken by multiple exposure. Based on the emulsion photosensitivity theory and experimental study[7], reciprocity law failure does not occur in the X-ray region. Therefore, multiple exposure would not affect the photosensitivity of the emulsion. An added benefit of multiple exposure is that the effect brought about from fluctuations of laser parameters is averaged out.

6

The Li-like silicon ion experiments were primarily carried out with the LF12 laser apparatus. In this work, only the southern-path laser beam was used in this dual-channel device. The energy of this 1.05-μm laser beam at the target is approximately 50 J, the relative fluctuation is under 10 percent, and the pulse width is around 900 ps. Due to the use of an array of cylindrical lenses, a focal line of uniform intensity was obtained: it was approximately 20 mm long and 130 μm wide. This is equivalent to a power density of 2×10^{12} W/cm^2 at the surface of the target. The target used was a 1-mm-thick polished silicon strip. The length of the linear plasma might be varied by changing the width of the silicon target. In this work, data was recorded on the single-grain-emulsion Kodak 101-01 film, which had been systematically calibrated prior to use. This special XUV film is not only very sensitive but also has very fine grains, low noise and fog. Hence, it is possible to obtain very good spectra. Experimentally, the hypertorus mirror was kept at 74 cm away from the focal line. The spatial magnification factor of the system is approximately 0.6. Even when the laser energy was as low as 30 J, a clear spectrum could be obtained after irradiating the target once.

III. Experimental Results

The ASE characteristics of the 5f-3d transition (105.7 Å) of the Li-like Al^{10+} ions was observed experimentally using a GIGS in the six-path laser facility[18]. Observation was made axially along the linear plasma, as well as off the axis. Along the axis, the 105.7-Å line was very obvious. Off the axis, however, the line disappeared into the background. As for the 5d-3p transition (103.8 Å) of Al^{10+}, it overlaps with other lines which made it impossible to obtain any quantitative results. At the same target laser power density, the axial spectra of five different lengths of plasma from five different width aluminum targets were obtained[18]. Based on the fact that the exposure of the X-ray film is linear with respect to the dark density D under low exposure conditions (D $\leqslant$ 0.5)[19-21], and after subtracting the intensity of the continuous background, it is possible to obtain the time-integrated relative intensity of the 105.7-Å line corresponding to any plasma length (as shown in Figure 5). The gain factor G is determined by the dependence of the line intensity upon the plasma length. The data is fitted into the following equation[22]:

$$I_{ASE} = I_0 \frac{(e^{GL} - 1)^{3/2}}{(GLe^{GL})^{1/2}}$$

where G is the gain factor, L is the length and I is the intensity. The gain factor thus obtained is 3.1 ± 0.9 cm^{-1} and the maximum gain length product is approximately 2.5.
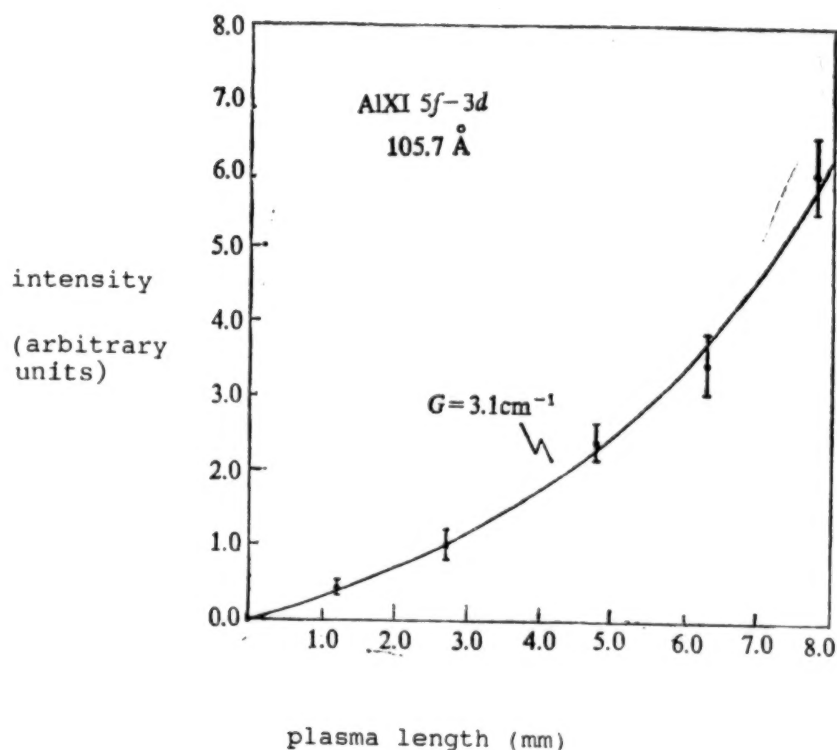
Figure 5. Gain Characteristic Curve: Intensity of 5f-3d transition of Li-like Al ions vs. plasma length

The soft X-ray emission spectra of the plasma at different positions away from the target could be obtained with the one-dimensional-spatial-resolution XUV grating spectrograph. Based on these space-resolved spectra, it is possible to obtain the spatial distribution of the gain of the 105.7-Å line. It was found that the maximum intensity occurred at approximately 440 m away from the target surface. An analysis pointed out that this corresponds to approximately 8 ns after the peak of the driving laser pulse. At that instance, the plasma has completely undergone adiabatic expansion and is in the process of rapid cooling, which is optimal for combination pumping.

The spectra taken by the T1AP crystal X-ray spectrograph showed that hydrogen-like ions essentially do not exist in the plasma. However, there is a relatively high concentration of helium-like ions. This indicates that the target laser intensity chosen is consistent with the combination pumping of Li-like ions.

In early 1989, a preliminary attempt was made to study the soft X-ray gain of Li-like ions using the six-path laser apparatus[18]. The gain factors of the Si^{11+} 88.9-Å (5f-3d) and 87.3-Å (5d-3p) transitions were

found to be 1.4 and 0.9 cm^{-1}, respectively, by measuring the axial to non-axial spectral intensity ratio. In August 1989, additional soft X-ray gain experiments were performed on Li-like Si ions using the LF12 laser facility. Because XUV-sensitive Kodak 101-01 film was used, a spectrum could be obtained by hitting the target once. Multiple exposure was not necessary. Figure 6 [photographs not reproduced] is a picture which shows typical marks left behind by a focused laser beam on the target. Figure 7(a) [photograph not reproduced] shows the XUV spectrum taken by the GIGS and Figure 7(b) shows the corresponding microdensitometer scan trace. A typical spectrum obtained by the PTGS is shown in Figure 8(a) [photograph not reproduced] and Figure 8(b) is the corresponding microdensitometer scan trace. By changing the width of the silicon target (9, 12, 15 and 18 mm), we obtained a series of axial spectra of various plasma lengths using the GIGS. Based on the calibration data for Kodak 101-01 film obtained by Kishimoto[23], the density of the spectral line could be converted into relative intensity. Figures 9 and 10 show the relative intensity as a function of plasma length for the 5f-3d (88.9-Å) and 5d-3p (87.3-Å) transitions of Si^{11+}, respectively, at 300 μm from the target surface. Using the above equation for I_{ASE}, the gain factors corresponding to 5f-3d and 5d-3p for Si^{11+} are 1.5 ± 0.5 cm^{-1} and 1.4 ± 0.5 cm^{-1}, respectively. The maximum gain length products are 2.7 and 2.5, respectively.
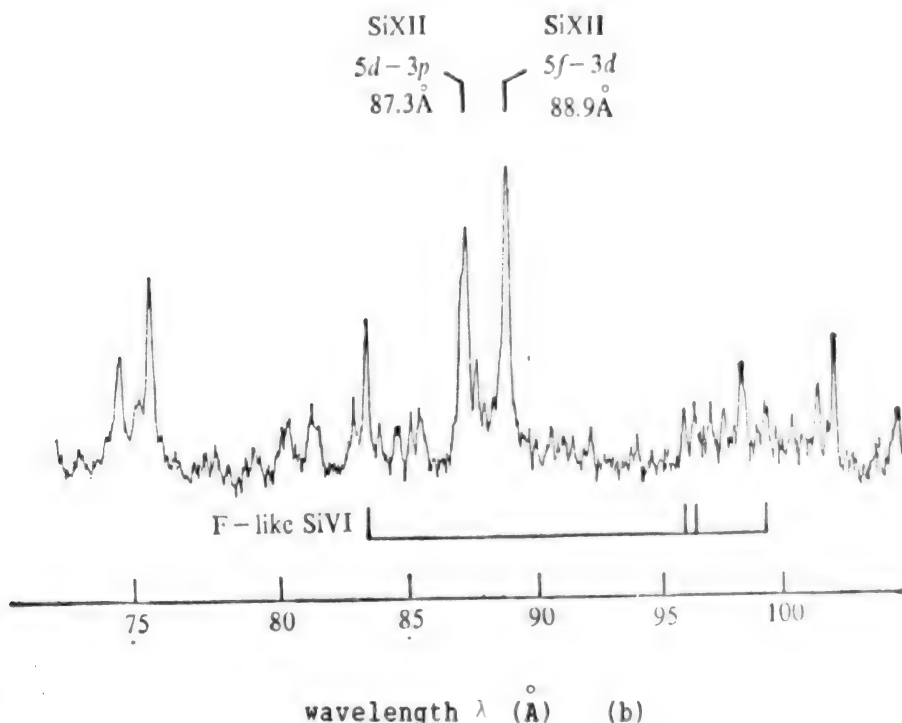

Figure 7. Axial XUV Spectrum of Linear Silicon Plasma (18 mm in length), taken on Kodak 101-01 Film with the GIGS: (a) photograph and the corresponding microdensitometer scan trace (b)

Continuum (SiXIII − SiXII)

SiXII ($4d − 2p$)

SiXII ($3d − 2p$)

SiXII ($5f − 3d, 5d − 3p$)

wavelength λ (Å)   (b)

Figure 8.   Axial X-Ray Spectrum of Linear Silicon Plasma (18 mm in length), taken on Kodak 101-01 Film with the PTGS (2000 lines/mm, 50-μm pinhole aperture, spectral resolution 2 Å) (a) and the corresponding microdensitometer scan trace (b)
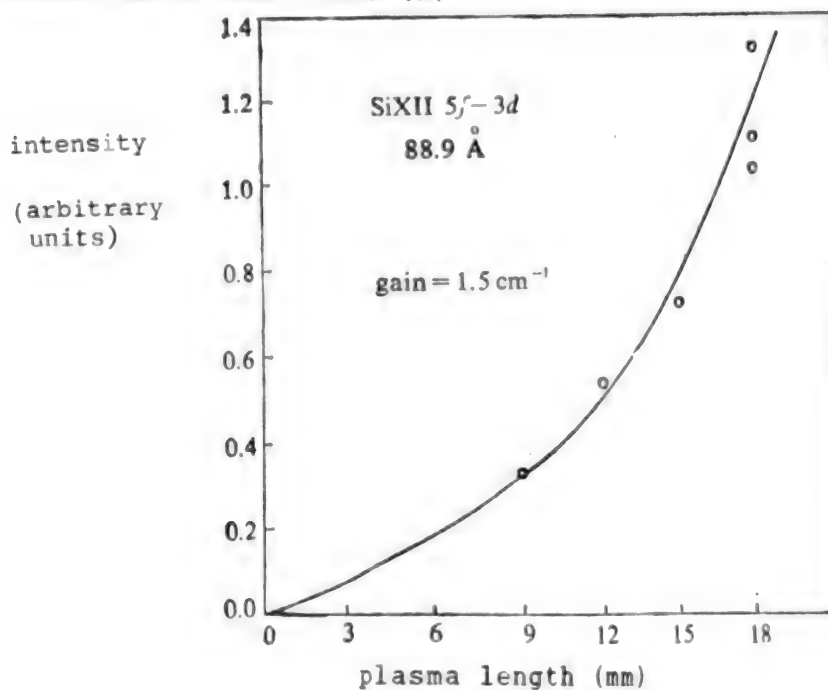

intensity

(arbitrary units)

SiXII $5f − 3d$
88.9 Å

gain = 1.5 cm⁻¹

plasma length (mm)

Figure 9.   Gain Characteristic Curve: Intensity of 5f-3d transition (88.9 Å) of Li-Like Si Ions vs. Plasma Length

10

intensity

(arbitrary
units)

SiXII $5d - 3p$
87.3 Å
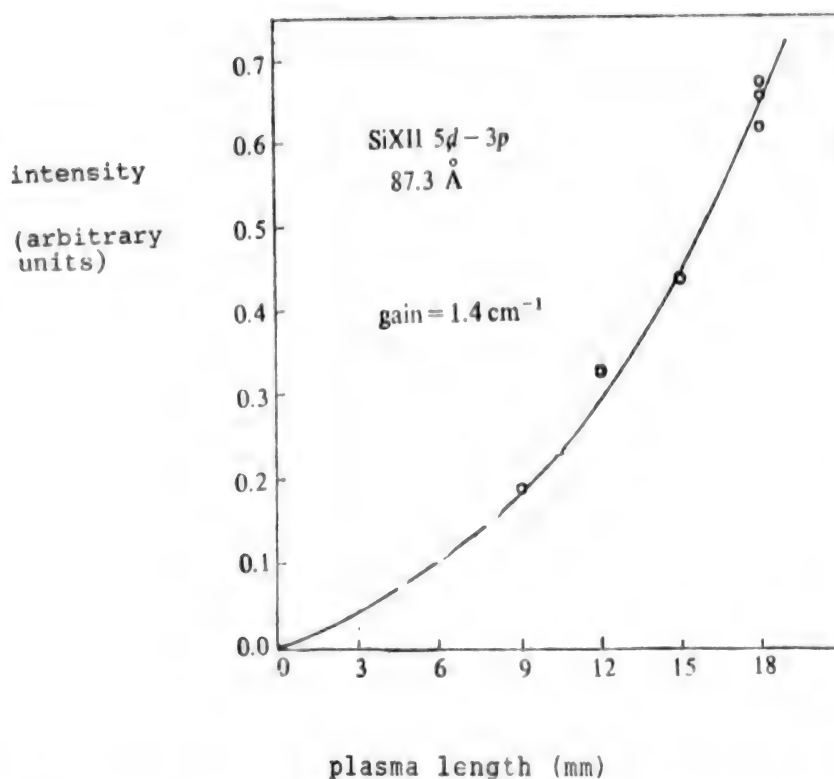
gain = $1.4 \, \text{cm}^{-1}$

plasma length (mm)

Figure 10. Gain Characteristic Curve: Intensity of 5d-3p Transition
(87.3 Å) of Li-Like Si Ions vs. Plasma Length

Although the soft X-ray gain measurement was mainly made with the high-
resolution GIGS, as an auxiliary diagnostic instrument, the PTGS also
provided some useful information.   The emission spectrum of the linear
plasma was recorded axially using the PTGS over the range of 5-200 Å.
On the LF12 laser apparatus, the transmission grating has 2000 lines per
mm and the spectral resolution is 2 Å.   A typical zeroth-order spectrum
(see Figure 8(a)) shows the track of silicon plasma spray along the
normal direction of the target surface.   The minimum transverse
dimension of the plasma was approximately 160 µm and the plasma spray
range was over 800 µm. In the microdensitometer scan trace of the
spectrum shown in Figure 8(b), the continuous spectrum near 20 Å
(Si^{12+} - Si^{11+} - combination radiation) indicates that there is a high
concentration of He-like ions in the plasma. This is obviously needed

11

in the pumping of Li-like ions. The spectrum also shows a strong peak near 44 Å corresponding to the 3d-2p transition of Si^{11+}. This indicates that in the laser transition (5f-3d), the lower energy level (3d) particles can be rapidly depleted. In addition, there is a distinct peak near 88 Å. However, due to limited resolution, it was not possible to distinguish the spectral lines corresponding to the 5f-3d (88.9-Å) and 5d-3p (87.3-Å) transitions of Si^{11+}. Therefore, it is difficult to quantitatively determine the PTGS results. A higher-resolution PTGS (such as using a grating with more lines per unit length) needs to be developed.

IV. Conclusions

Soft X-ray lasing from combination-pumped Li-like aluminum and silicon ions has been successfully demonstrated. In this work, laser gain of the 5f-3d and 5d-3p transitions of the Li-like Si^{11+} ions has been observed for the first time. The wavelength of the soft X-rays is shorter than 100 Å. It is especially significant that the results were obtained at a low pumping laser power density. Our study shows that it is feasible to push the X-ray laser to the "water window" band (43.8 - 23.2 Å) using the Li-like combination mechanism on our existing laser facility.

References

1. Matthews, D. L., et al., PHYS. REV. LETT., 54(1985), 110.

2. Suckewer, S., et al., ibid., 55(1985), 1753.

3. Lee, T. N., McLeau, E. A. & Elton, R. C., ibid., 59(1987), 1185.

4. MacGowan, B. J., et al., ibid., 59(1987), 2157; JOSA., B5(1988), 1858.

5. Chenais-Popovics, C., et al., PHYS. REV. LETT., 59(1987), 2161; Carillon, A., et al., Central Laser Facility Annual Report, Rutherford Appleton Laboratory, 1987, 13.

6. Kiehn, G. P., et al., SPIE., Vol. 831, X-ray from laser Plasmas, 1987, 270.

7. Jaeglé, P., et al., J. PHYS. B: At. Mol. Phys., 18(1985), 4647.

8. Jamelot, G., et al., IEEE., TRANSACTIONS ON PLASMA SCIENCE, 16(1988), 497.

9. Herman, P. R., et al., ibid., 16(1988), 520.

10. Hara, T., et al., JAPANESE J. APPL. PHYS., 23(1989), L1010.

11. Kim, D., Skunner, C. H., JOSA., B6(1989), 115.

12. Xu Zhizhan, et al., CHINESE PHYS., 1, 548, 1981.

13. Deng Ximing, et al., "Report of Shanghai Institute of Optics and Fine Mechanics," Academia Sinica, Shanghai, 1987.

14. Xu Zhizhan, et al., OPT. COMM., 69, 49, 1988; PHYS. REV., A39, 808, 1987.

15. Zhang Baiquan [1728 4101 3123], et al., GUANGXUE XUEBAO [ACTA OPTICA SINICA], 8, 762, 1988.

16. Pachtman, A., et al., in "Proceedings of the Second Symposium on Plasma-Wave and Plasma-Matter Interaction," Association for Plasma Studies of China Report No. APS-88-006, paper D-1, November 1988.

17. Mees, C. E. K. & James, T. H., Theory of Photographic Process (Chinese Translation), Science Publishing House, 1979.

18. Xu Zhizhan, et al., ZHONGGUO JIGUANG [CHINESE JOURNAL OF LASERS], 16, 385, 1989.

19. Blokhin, M. A., in "Methods of X-ray Spectroscopic Research," Pergamon Press, 1965.

20. Fan Pinzhong and Mao Chusheng [3029 2806 3932], GUANGXUE XUEBAO [ACTA OPTICA SINICA], 4, 956, 1984.

21. Lewis, C. L. S. & Mahoney, E. R., J. PHYS. E: SCI. INSTRUM., 17(1984), 744.

22. Linford, G. J., et al., APPL. OPT., 13(1974), 397.

23. Kishimoto, T., Report of Max-Plansk-Institut, für Quantenoptik, Garching, 108, 1985, 70.

General-Purpose Programmable Digital Radar Signal Processing System

[Article by Peng Yingning [1756 2019 1337], Yan Mingsheng [7051 7686
3932] of the Dept. of Information and Electronics, Qinghua University,
Beijing; for earlier report, see JPRS-CST-89-004, 2 Feb 89, pp 75-76]

[Text]   Abstract

A recently developed multi-function programmable digital radar signal
processing system is described. The system is composed of an adaptive
moving target indicator (AMTI) with variable number of pulses, a digital
pulse compression unit (DPC), a moving target detector (MTD), a digital
integrator (DI) and a constant false-alarm rate (CFAR) processor. The
mode of operation and the parameters of the system can be assigned or
changed from a program or from interactive commands via the radar
computer. The system is also equipped with advanced BITE [built-in test
equipment] which can detect and isolate faulty elements on a particular
circuit board. Test results indicate that the average noise improvement
factors of the system for suppressing ground clutter and weather clutter
are greater than 53 dB and 40 dB respectively, and the sidelobe level of
the DPC is less than -40 dB. By using innovative algorithms and
advanced hardware and architecture, the operational speed of the system
has been increased to 1148 MIPS [million instructions per second]. This
system can be used on many advanced three-coordinate and two-coordinate
radar systems.

I.   Introduction

An advanced radar signal processing system should have the following
capabilities: fast response to rapid changes in radar waveforms;
adaptive suppression of strong interference effects such as ground
clutter, weather fluctuations, and chaff; good CFAR performance under
different clutter environment; programmability to accommodate changes in
the environment and in system parameters and mode of operation. The
multi-function general-purpose programmable radar signal processing
system described in this article can meet all these requirements.

This newly developed system can operate in seven different modes with dozens of different parameters. Fig. 1 shows the system block diagram, which includes the following functional blocks:

(1) A 12-bit four-channel A/D converter which converts orthogonal diversity signals.

(2) An AMTI which can operate with 2, 3, 4 or 6 pulses; each has several selectable notch positions. The notch coefficients can be keyed in from the panel or assigned or changed from radar computer commands.

(3) The DPC unit consists of FFT [fast Fourier transform] array processors and the associated controllers and floating-point/fixed-point converters; it can perform the functions of both digital linear and non-linear frequency-modulation pulse compression.

(4) The MTD consists of a Doppler filter bank and a bank of controllers; it can perform the operation of 4th, 6th and 8th-order FIR [finite-impulse-response] filters.

(5) The I and Q channel modulo circuit.

(6) When the DI detects the presence of wideband active interference, it emits continuous pulses in the direction of interference in the PC+DI mode.

(7) Frequency-diversity synthesis is applied to the F_1 and F_2 signals.

(8) The noise σ is estimated using a retrace or fixed-interval estimation technique to establish the adaptive threshold for the CFAR processor.

(9) The σ of weather clutter is estimated by unit averaging and is used for CFAR processing; the number of averaging units can be chosen arbitrarily.

(10) The clutter chart is used to detect the target in the tangential direction and to establish the clutter CFAR threshold. The recursion coefficient of the clutter diagram can be 1/4, 1/8 or 1/16.

(11) The five-phase system clock is provided by a 20-MHz crystal oscillator.

(12) The controller is a 2900-series bit-slice microprogram controller.

(13) The BITE can perform on-line self-diagnosis, and indicate the fault location. By applying the characteristic word-compression analysis technique and using pseudo-random code as the test source[1], the amount of BITE hardware is reduced, and the diagnosis success rate and the fault location rate reach 99.9 percent.

(14) The input/output interface exchanges data and commands with the radar computer.

This system achieves a high degree of flexibility by incorporating the key signal-processing techniques used in modern radars. It contains 35 circuit boards and 2100 integrated circuits; its power consumption is 280 watts. The main modules of the system--the AMTI, the DPC, and the MTD--will be described in more detail in the following sections.
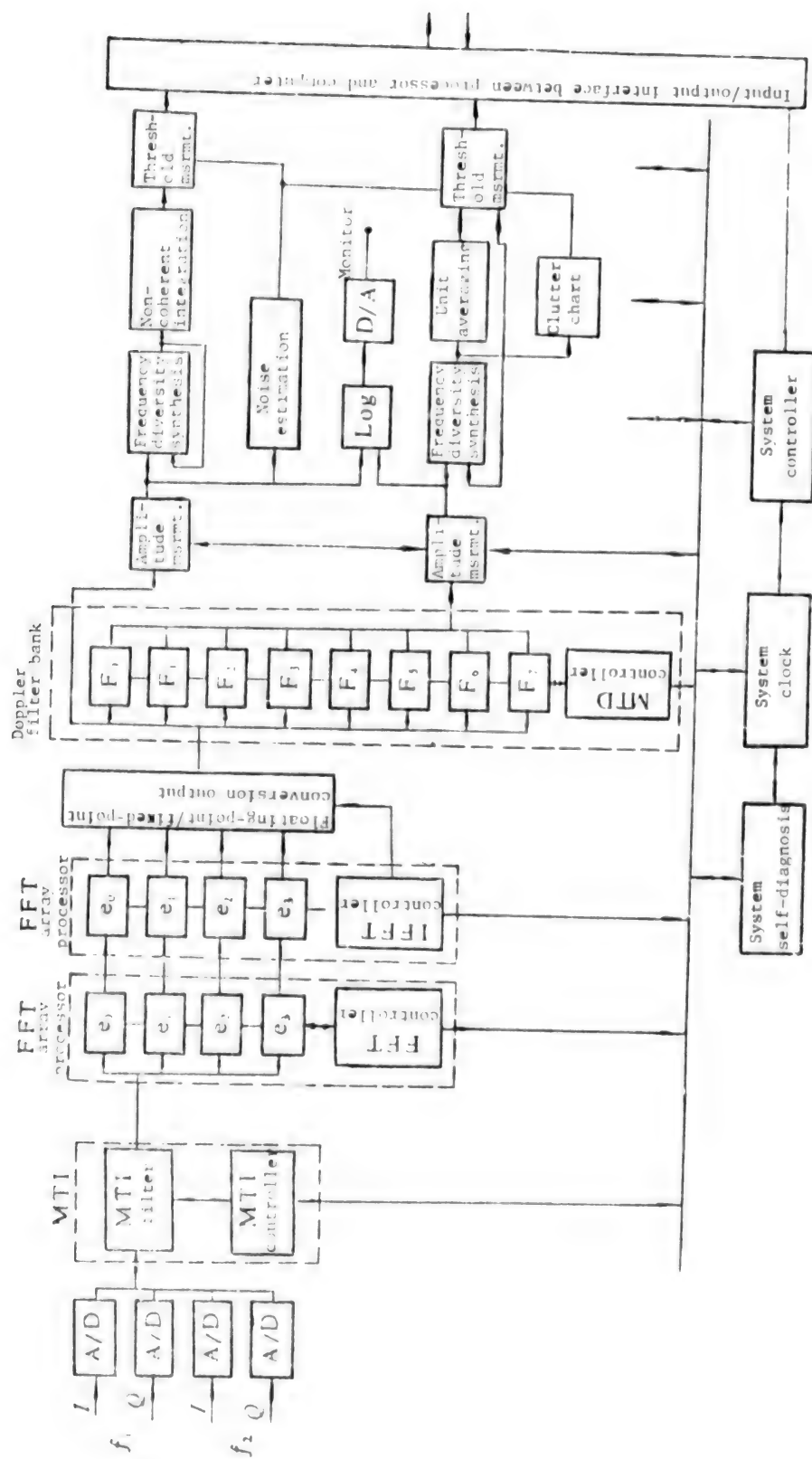
Figure 1   System block diagram

18

II. Adaptive MTI

The number of pulses and the position of the notch center can be varied according to the clutter environment. The system uses a "trial and error" AMTI technique[2] whose procedure is as follows. Prior to processing, "optimum" MTI weighting coefficients designed to suppress a wide range of clutter waveforms are stored in the processor. The first step is to try various weighting coefficients on each resolution element; the set of coefficients which yield the smallest clutter residual is selected as the weighting coefficients for the next time segment. The trial is repeated periodically to ensure that the MTI remains in its "optimum" state required for adaptive clutter suppression.

The three-pulse MTI is divided into five range segments; each segment has 11 notch centers: 0 Hz, ± 25 Hz, ± 50 Hz, ± 75 Hz, ± 100 Hz, and ± 125 Hz. Notch width is 50 Hz. The four-pulse MTI is divided into three range segments. The six-pulse MTI has one range segment with five notch centers: 0 Hz, ± 50 Hz, and ± 100 Hz; notch width is 200 Hz.

The three-pulse MTI is used for suppressing ground clutter or weather clutter; the four-pulse MTI is used for suppressing strong ground clutter; the six-pulse MTI is used for suppressing simultaneous ground and weather clutters; and the two-pulse MTI is used in conjunction with a Doppler filter bank to form the MTD for suppressing more complex clutter.

(A) Design of Staggered MTI Weighting Coefficients

In this paper, two design methods for staggered MTI weighting coefficients are introduced; the resulting staggered MTI noise improvement factor approaches the optimum improvement factor of non-staggered MTI.

1. MTI Weighting Coefficient Correction Method

Let the optimum weighting coefficients of non-staggered MTI be $\{a_n\}$ (n=0, 1, ..., N-1); its frequency response is:

$$H_a(f) = \sum_{n=0}^{N-1} a_n e^{-j2\pi f n T},$$ (1)

where T=1/PRF [pulse repetition frequency] is the pulse repetition interval.

In the case of staggered pulses, let the transmission time of the nth pulse be T_n, and the time-varying weighting coefficients be $\{W_n\}$; then the frequency response of the staggered MTI is:

$$H_w(f) = \sum_{n=0}^{N-1} W_n e^{-j2\pi f T_n}$$

(2)

In the coefficient correction method, corrections are made to the coefficients $\{a_n\}$ to generate the time-varying weighting coefficients $\{W_n\}$. Let:

$$|H_a(f)|^2 \simeq |H_w(f)|^2 \quad |f - f_0| \leqslant PRF/2$$

(3)

where f_0 is the clutter center frequency. First consider the case $f_0 = 0$; by expanding both sides of equation (3) in a Taylor series about zero, we obtain:

$$H_a^{(m)}(0) = H_w^{(m)}(0), \quad m = 0, 1, \cdots, N-2$$

(4)

Substituting equations (1) and (2) into equation (4) gives (N-1) linear equations; the additional normalizing equation yields a total of N equations:

$$\begin{cases} \sum_{n=0}^{N-1} T_n^m W_n = \sum_{n=0}^{N-1} (nT)^m a_n \\ \sum_{n=0}^{N-1} |W_n|^2 = \sum_{n=0}^{N-1} |a_n|^2 \end{cases}$$

(5)

The corrected time-varying weighting coefficients are obtained by solving equation (5).

When $f_0 \neq 0$, one obtains from equation (2):

$$\begin{cases} \widetilde{H}_w(f) = H_w(f - f_0) = \sum_{n=0}^{N-1} \widetilde{W}_n e^{-j2\pi f T_n} \\ \widetilde{W}_n = W_n e^{j2\pi f_0 T_n}, \quad n = 0, 1, \cdots, N-1 \end{cases}$$

(6)

Substituting W_n into the above equation gives the time-varying weighting coefficients for staggered MTI when the notch center frequency is not zero.

The correction procedure can be summarized as follows:

(1) design the optimum weighting coefficients $\{a_n\}$ for the case of non-staggered MTI and zero notch center frequency; (2) solve equation (5) to obtain the time-varying weighting coefficients $\{W_n\}$ for staggered MTI; (3) the weighting coefficients $\{\widetilde{W}_n\}$ for non-zero notch center frequency can be obtained from equation (6).

The weighting coefficient correction method is applicable only in a simple clutter environment; when multiple clutter waveforms are present, the eigenvector method should be used.

2. Eigenvector Method

The eigenvector method is a direct design method of optimum MTI weighting coefficients when the inter-pulse stagger code is known; the basic principle behind this method is to maximize the average noise improvement factor for a known clutter model.

Let the staggered MTI time-varying weighting coefficients be $\{W_n\}$, then its frequency response is:

$$H_w(f) = \sum_{n=0}^{N-1} W_n e^{-j\omega T_n}, \quad n = 0, \ 1, \ \cdots, \ N-1$$

(7)

where $\omega = 2\pi f$. Let the clutter power spectrum be $c(f) = \sum_{i=1}^{m} c_i(f)$, where $c_i(f)$ are the power spectra for ground clutter, weather clutter, chaff, noise, etc.; the clutter correlation matrix is $C = [C_{ij}]$.

$$C_{ij} = \frac{1}{2\pi} \int_{-\infty}^{+\infty} C(f) e^{-j2\pi(t_i-t_j)f} df$$

(8)

The Doppler frequencies of the signal are generally assumed to be uniformly distributed within the range of MTI velocity response; hence they have a uniform power spectrum $S(f)$

$$S(f) = \begin{cases} 1 & \text{for } f_1 \leqslant |f| \leqslant f_2 \\ 0 & \text{otherwise} \end{cases}$$

f_1, f_2 are the upper and lower bounds of the frequency response. The signal correlation matrix is $S = [S_{ij}]$, where

$$S_{ij} = \begin{cases} [\sin 2\pi f_2(T_i - T_j) - \sin 2\pi f_1(T_i - T_j)]/2\pi(f_2-f_1)(T_i - T_j), & i \neq j \\ 1 & i = j \end{cases}$$

When the range of the staggered MTI velocity response is very wide, one can assume $f_2 \to \infty$, $f_1 \to 0$, and the signal correlation matrix becomes a unit matrix $S = I$, and the improvement factor is:

$$I_{ic} = \frac{W^T W^*}{W^T C W^*}, \quad W = \{W_i\}$$

(9)

21

Thus, the problem of finding the optimum weighting reduces to one of finding the eigenvector which corresponds to the smallest eigenvalue of the matrix C; i.e., we must solve the equation:

$$CW^* = \lambda W^*$$

(10)

where λ is the eigenvalue of the matrix C. When $\lambda = \lambda_{min}$,

$$I_{s/c} = I_{s/c\,max} = \frac{1}{\lambda_{min}}$$

(11)

Fig. 2 shows the frequency response of a staggered six-pulse MTI design based on the eigenvector method. The figure shows a deep notch at 0 Hz, and a 200-Hz-wide notch extending from -50 Hz to 150 Hz; also, the ripples within the passband are quite small. Therefore, this design can simultaneously suppress ground clutter and weather clutter whose center frequency falls in the range from -50 Hz to 150 Hz. Table 1 shows a comparison of the noise improvement factors for four different weighting coefficients of a six-pulse MTI; the clutter is assumed to have a Gaussian spectrum, and the PRF is 657 Hz.
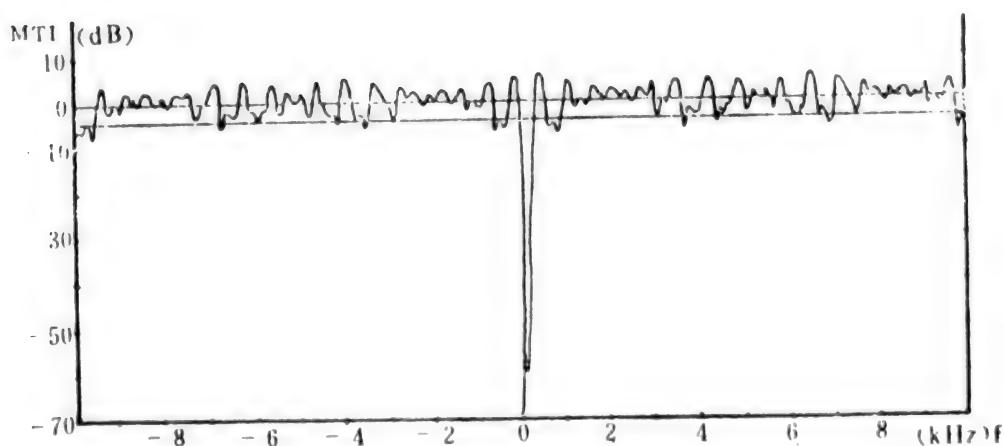

Fig. 2   Synthesized Frequency Response of a Staggered Six-Pulse MTI

22

Table 1 Average Improvement Factors of Six-Pulse MTI

	Clutter center frequency and spectral width		
	$f_0 = 0$Hz $\sigma = 4$Hz	$f_0 = 0$Hz $\sigma = 13$Hz	$f_0 = \pm 25$Hz $\sigma = 13$Hz
Non-staggered optimum weighting	64.6	54.1	47.9
Staggered coefficient correction weighting	64.7	53.9	47.4
Staggered optimum weighting (eigenvector)	64.7	53.8	47.5
Staggered uncorrected weighting	54.3	44.5	38.6

One can see from Table 1 that if the coefficients of staggered MTI are not corrected, the improvement factor will be 10 dB lower than that of non-staggered optimum weighting.

(B) Performance Tests of AMTI

Performance tests of AMTI have been conducted using simulated clutter and signal sources. The clutter is assumed to have a Gaussian spectrum with $\sigma = 4$ Hz for ground clutter and $\sigma = 13$ Hz for weather clutter. Test results of average noise improvement factors and velocity response indices are shown in Table 2 and Table 3, respectively.

Table 2 Average Improvement Factors of AMTI

Number of pulses	3		4	6	
Clutter type	Ground	Weather	Ground	Ground	Weather
$\overline{SCI}$ (dB)	54	40.2	58	58.5	47.6

Table 3 Velocity Response Indices of AMTI

Number of pulses	3	4	6
Range of velocity response (km/h)	54→5485	60→4061	58→4938
Minimum intra-passband response (dB)	−5.8	−7	−7.07
Percentage of intra-passband responses below −4dB	3.8	10.3	9

23

III. Digital Pulse Compression

The system can perform digital pulse compression of linear frequency-modulated (LFM) signals. The waveform parameters of pulse compression are given in Table 4.

Table 4 Waveform Parameters of DPC

T pulse width (μs)	B bandwidth (MHz)	BT	R_{max} (km)
32	1	32	⩽200
64	1	64	⩽200
64×2	0.5	32	⩽200 (frequency diversity)
320	0.8	256	200~500
640	0.8	512	200~500
640×2	0.4	256	200~500 (frequency diversity)

As shown in Fig. 3, DPC is accomplished using fast convolution, which involves FFT, spatial frequency-domain weighting, and inverse FFT [IFFT]. The weighting function is the complex conjugate of the FFT of the transmitted LFM waveform multiplied by a generalized Hamming weighting factor.

Fig. 3 DPC Implementation

(A) Sampling rate of LFM digital pulse compression and frequency-domain weighting

The expression for a digitized LFM return wave is:

$$S(n) = A \cdot \exp\left\{ -j2\pi \left[f_d(n-x) T_s + \frac{B}{2T} \cdot (n-x)^2 T_s^2 \right] \right\} \cdots \tag{12}$$

24

where T is the pulse width, B is the bandwidth, f_d is the Doppler frequency, $T_s = 1/PB$ is the sampling period, and x is the initial sample value ($0 \leqslant x \leqslant 1$). Let $t = (k - x)\frac{T}{M}$, $|k| \leqslant M-1$, $M = 1/T_s$, $r = f_d T$, $N = TB$.

Then the ambiguity function of digital pulse compression is:

$$\left| A_d \left(t = (k+x)\frac{T}{M}, \ f_d = \frac{r}{T} \right) \right| = \frac{\sin \pi (N/M)\left(k+x-\frac{M}{N}r\right)(1-|k|/M)}{\sin \pi (N/M^2)(k+x-M/N\cdot r)} \cdots \quad (13)$$

$|A_d (t, f_d)|$ is a periodic function on the frequency axis with period $1/T_s$. When p = 1, the periodicity of the function produces false sidelobes in the neighborhood of $|t| = T$. In the past, this problem has often been solved by increasing the sampling rate (let $f_s = 1/T_s = B + f_{d\,max}$); but when the sampling is mismatched (when x is large), the value of x folded onto f_d may be greater than $f_{d\,max}$ (because in equation (13), the effects of x and f_d are equivalent). Therefore, the false sidelobes cannot be eliminated by this method; the best method for eliminating false sidelobes is the frequency-domain weighting method. When the weighting process reduces all the sidelobe levels to below a standard value, then the false sidelobes can be completely eliminated even when the sampling rate f_s is equal to B. Computer simulation results show that the generalized Hamming weighting can produce low sidelobes with small weighting loss. The weighting function is:

$$w(k) = a + (1-a)\cos(2\pi k/N), \quad (k = 1, \ 2, \ \cdots, \ N)$$

When a = 0.54, the actual pulse-compressed waveforms are as shown in Fig. 4 [photographs not reproduced], where the conditions are: p = 1, x = 0 (corresponding to zero target distance), $f_d = 0$. Fig. 4a is for BT = 256, Fig. 4b is for BT = 512; the horizontal axis is time and the vertical axis is amplitude whose scale is 10 dB/div. The photographs clearly show that the pulse-compressed sidelobes are less than -40 dB.

(B) Block Floating-Point Algorithms in Pulse Compression

Since pulse compression is accomplished using FFT, the FFT algorithms will greatly affect the accuracy, linear dynamic range and speed of pulse compression. The traditional FFT uses fixed-point algorithms to avoid overflow, but this reduces the linear dynamic range due to the loss of weak signals. The ideal approach is to use all floating-point algorithms, but this approach results in higher cost and significantly lower speed. A compromise is to use block floating-point algorithms. The speed of block floating-point algorithms is close to that of fixed-point algorithms, and their linear dynamic range is significantly higher with a penalty of only a small amount of additional hardware. Computer simulation results show that the linear dynamic range of a 12-bit-word block floating-point pulse compression is the same as that of a 20-bit-word fixed-point pulse compression. The system maintains good linearity

over a range of input values from 2 bits to 10 bits. The average error
of a 12-bit-word block floating-point algorithm compared to an infinite-
word fixed-point algorithm is: $\bar{\Delta} = 0.16\%$ when BT = 64, and $\bar{\Delta} = 0.23\%$
when BT = 256.

(C) Hardware implementation of Digital Pulse Compression

The core of the DPC hardware is the FFT module, which consists of an
array of arithmetic units to achieve higher speed for both FFT and IFFT
in order to meet real-time requirements. The number of arithmetic units
in the array, m, should satisfy the condition $m = 2^s$ (s is a positive
integer); this system has eight arithmetic units, with m = 4. This
array can perform DPC with any number of points n (n $\gtrless 2^m$, and $n = 2^r$)
without having to change hardware configuration . Fig. 5 shows the
data-exchange network between the FFT and IFFT arithmetic units; four of
the arithmetic units operate synchronously, and therefore can share the
same controller. In the figure, the BU_i's are the arithmetic units, and
S_{ii} and S_{ji} are the storage units. The only difference between FFT and
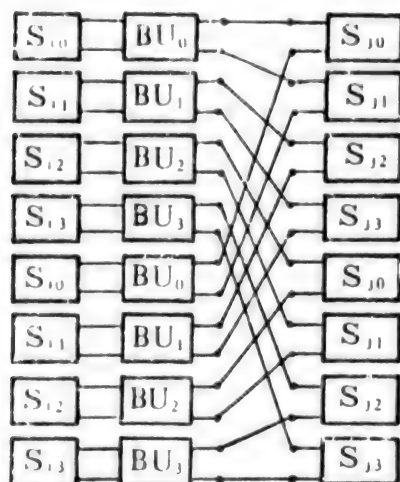IFFT is in the contents of the coefficient storage units.

Fig. 5 Array of Arithmetic Unit for FFT and IFFT

The measured speeds of digital pulse compression are presented in
Table 4, which shows that the actual processing times are all less than
one half the FFT data window length. Table 5 presents the measured
performance indices of pulse compression.

Table 4 Processing Times of LFM Pulse Compression for Different BT Values

Signal BT	No of FFT points	Window length(µs)	Actual processing time (µs)
32	64	64	27.3
64	128	128	56.8
256	512	640	2?5.0
512	1024	1280	?63.?

Table 5 Measured Indices of DPC

BT	32	64	256	512
Sidelobe level (dB)	-20	-20	-30	-42
Linear dynamic range (bits)	9	9	9	9
Aver. linearity error (%)	2.9	1.3?	1.82	1.76

It is seen from Table 5 that for BT = 256 and 512, the DPC sidelobe level is less than -40 dB; over all BT values, the linear dynamic range of the system is 9 bits, and the error in linearity is less than 3 percent.

IV. Variable-Step MTD

The MTD mode of operation is designed for a highly complex clutter environment; the number of pulses can be varied between 4, 6 or 8. There are six modules in the MTD: the two-pulse cancellation unit, the narrow-band FIR filter bank, the zero-velocity filter [ZVF], the modulo unit, the frequency-diversity summation unit and the MTD-CFAR unit.

By using two-pulse cancellation, the pre-MTD suppresses most of the ground clutter, and therefore reduces the dynamic range requirements on pulse compression [PC] and on the Doppler filter bank. The basic principle of the MTD is shown in Fig. 6.
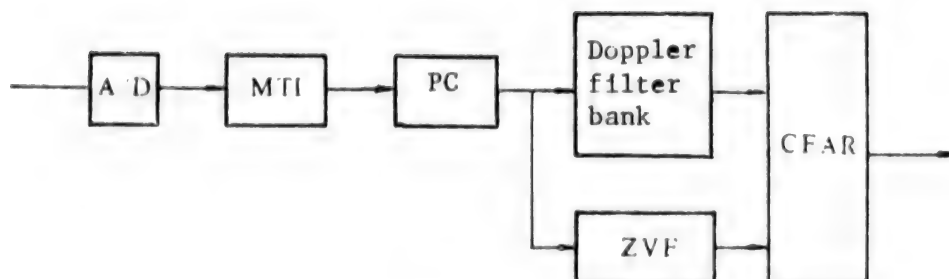
Fig. 6 MTD Block Diagram.

Let the number of pulses of MTD be N, then the zero-velocity filter ZVF
and the (N-1) Doppler filters constitute a total of N filters. The ZVF
is a low-pass filter, which filters out the ground clutter and stores it
in the 1-Mbyte clutter chart to be used as threshold for detecting
tangential targets and as the CFAR threshold in the non-zero-velocity
Doppler channel. Since the return wave has already lost most of the
ground clutter as it passes through the MTI, it must be recovered in ZVF
processing. This is accomplished by making corrections to the ZVF
weighting coefficients. Let the weighting coefficients of the ZVF
filter before correction be h_n (n = 0, 1,..., N-1), and let the
corrected coefficients by W_n, then:

$$W_n = \sum_{i=0}^{N-1} 2h_i$$

By correcting the weighting coefficients of the ZVF to W_n, the ground
clutter eliminated by the MTI can be recovered. The structure of the
ZVF is identical to that of each filter in the Doppler filter bank, and
they are synchronized in time; as a result, the MTD controller is
greatly simplified.

The design of the filter bank is accomplished using the optimized Remez
multiple-transform algorithm; the center positions of the filters are
distributed at unequal intervals, and the sidelobe levels are also
different. The hardware of the MTD filter bank consists of 8 identical
arithmetic boards and 1 control board. When operating as a 8-pulse MTD,
all 8 arithmetic boards are used; when operating as a 6-pulse MTD, only
the ZVF and boards F_1-F_5 are used; when operating as a 4-pulse MTD, only
the ZVF and boards F_1-F_3 are used.

The number of pulses of MTD and the weighting coefficients can be
changed locally from the keyboard or by radar computer commands.

The modulo unit, the CFAR unit and the clutter chart of the MTD are
quite simple and will not be discussed here.

28

Table 6 shows the test results of the average MTD noise improvement factors; the test conditions are as follows: the clutter is assumed to have a Gaussian spectrum, the ground clutter has a σ of 4 Hz and an amplitude of 66 dB; the weather clutter has a σ of 13 Hz and an amplitude of 48 dB.

Table 6   MTD Average Noise Improvement Factors

No of MTD pulses	8		6		4
Clutter type	Ground	Weather	Ground	Weather	Ground
Aver. Improvement factor $\overline{SCI}$ (dB)	58.5	44.3	53.7	42.5	46.8

It is seen from Table 6 that except for the 4-pulse MTD, the $\overline{SCI}$ for ground clutter is greater than 53 dB, and the $\overline{SCI}$ for weather clutter is greater than 42 dB.

V.   Concluding Remarks

The main features of this newly developed multi-function programmable radar digital signal processing system are: high performance, wide range of capabilities, ultra-high-speed real-time calculation and highly flexible programmability. The arithmetic speed indices are presented in Table 7, which corresponds to an overall operating speed of 1148 MIPS. Such high arithmetic speed is achieved by using advanced architecture (array and parallel processing), effective control design (multiple instruction stream/multiple data stream [MIMD], bit-slice microprogramming), and ultra-high speed components (55-ns MAC, 45-ns RAM etc.).

Table 7   Arithmetic Speeds of Different Modules

Name of module	MTI	DPC	Filter bank	Modulo unit	Unit averaging	Detection	Output buffer	Total
Arithmetic speed (MIPS)	24	848	192	22	26	33	3	1148

A single-board computer is used to perform the functions of monitoring, fault comparison, local editing, coefficient loading and modification, and operational control for the entire system.

The system is highly stable and reliable, and can be used on both three-coordinate and two-coordinate radar systems with different parameters.

References

1. Ma Dawei, Peng Yingning, Ma Zhang-e, "A New Internal Test Equipment for Digital Systems", CCSP-88-Proceedings, pp 960-961, Xian

2. J. L. Perry, "Clutter-Suppression Techniques on an Electronic Scanning Radar," G.E. Co., 1979.

3. Yan Ming Sheng, Mao Yuhai, "Design of Staggered MTI Weightings in Multi-Clutters," CIE 1986, International Conference on Radar, Beijing, China, pp 375-380.

Eleven-Meter-Antenna Earth Station for Domestic Satcom System

[Text] Abstract

The 11-m-antenna satcom earth station developed by Institute 1 of the Ministry of Posts and Telecommunications (MPT) is primarily used for domestic satellite communications, but it can also be used for international satcom systems. The earth station uses all-Chinese-made components and equipment, whose performance indices meet the national standards; it is one of the turn-key earth stations developed by this country in recent years. In April 1989, MPT organized a team of experts and technical personnel to test the earth station for certification. The results showed that this earth station is superior to earlier stations in terms of technological maturity and system integrity. In addition, in terms of performance-to-cost ratio, usability, and maintainability, it is far superior to imported facilities; it is expected that Chinese-built earth stations will gain greater acceptance by the users.

1. Earth Station System

The design and performance of the 11-m-antenna earth station meet the "Overall Technical Requirements for Domestic Satellite Communications Earth Stations" of the "National Standards". The overall system block diagram is shown in Fig. 1.
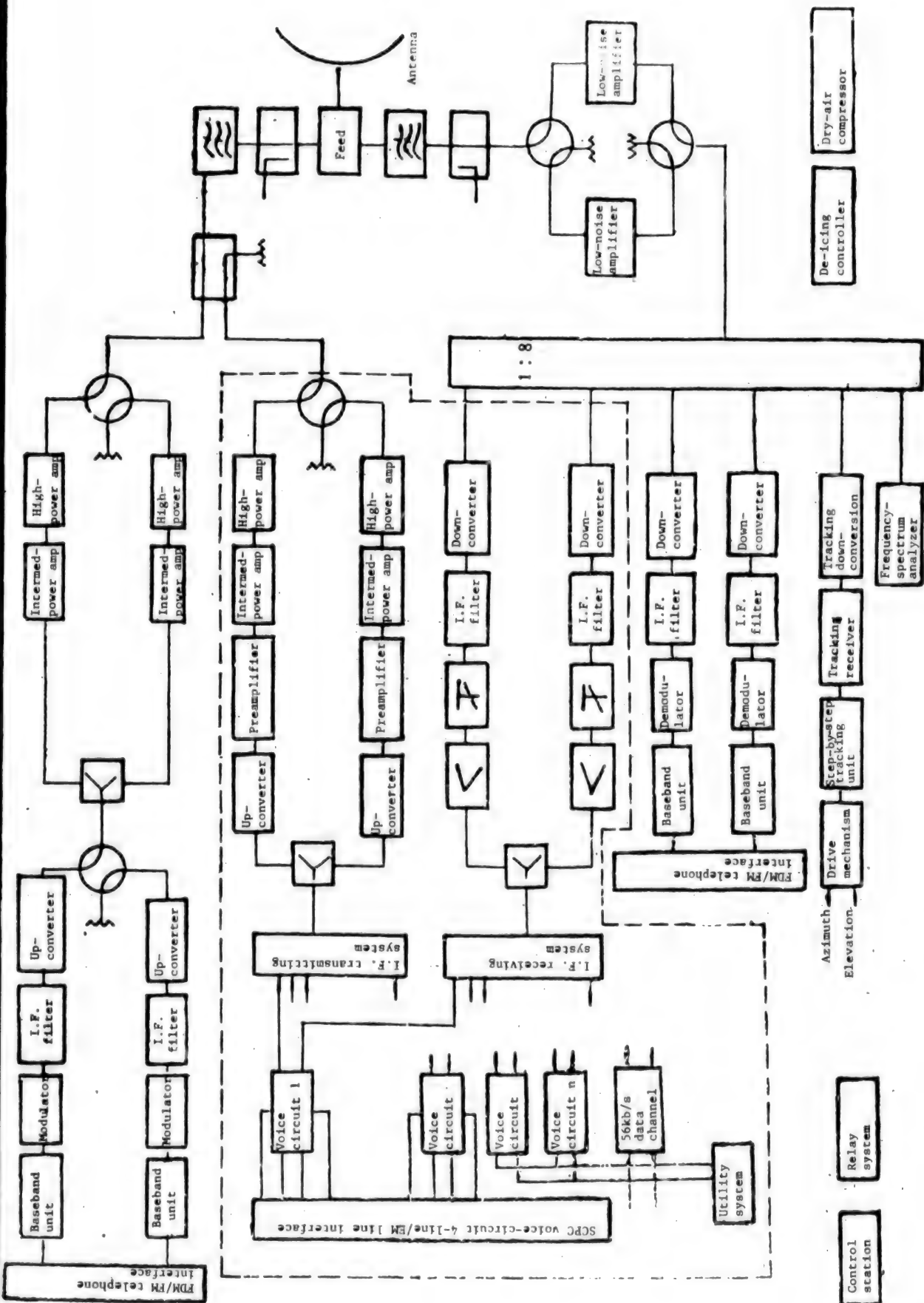
Fig. 1. System Block Diagram of FDM/FM, SCPC Earth Station

1.1. System Components

This system contains the following subsystems:

Antenna-feed subsystem

High-power amplifier subsystem

Low-noise amplifier subsystem

FDM/FM [frequency division multiplexing/frequency modulation] ground
communications equipment subsystem

SCPC [single channel per carrier] ground communications equipment
(including up/down frequency converter and terminal equipment)

System control and monitoring subsystem

Power supply subsystem

It is a practical and complete earth station which has a typical system
configuration and uses the two primary modes of communication commonly
used for domestic satellite communications--FDM/FM and CVSD/PSK/SCPC
[continuous variable slope delta modulation/phase shift keying/single
channel per carrier]

The monitoring and control (MAC) system is computer-controlled and has an
advanced design with special emphasis on system reliability.

1.2. Overall Technical Performance

Antenna diameter	11.6 m
Receiving gain	51.6 dBi
Transmitting gain	54.9 dBi
Sidelobe characteristics	meets CCIR specifications
Earth station G/T [figure of merit]	31.7 dB/K
System operating frequency range	
transmit	5.925-6.425 GHz
receive	3.700-4.200 GHz
Power stability	$\leqslant \pm 0.5$ dB/24 hours
Frequency stability	$\leqslant \pm 250$ Hz
RF out-of-band emission	$\leqslant 4$ dBW/4 kHz
RF intermodulation product	$\leqslant 21$ dBW/4 kHz
FDM/FM capacity	24 ch - 972 ch
S/N [signal-to-noise ratio] (for specified C/N [carrier-to-noise ratio])	$\geqslant 50$ dB
SCPC (data) bit error rate (BER)	
C/N = 15.5 dB	$\leqslant 1 \times 10^{-6}$
C/N = 13.5 dB	$\leqslant 1 \times 10^{-4}$
C/N = 13.5 dB (with FEC [forward error correction])	$\leqslant 1 \times 10^{-7}$

1.3. Description of System Components

Antenna. The antenna is of Cassegrain design with an aluminum reflector. The design not only has very high reflector efficiency but also meets strict sidelobe requirements (29-25 log θ). In addition, a step-by-step tracking system developed by this institute is also used.

High-Power Amplifier. High-power amplification is accomplished by a 3000-W klystron power amplifier; the drive stage is a 1-W FET (field effect transistor) amplifier located in the same container. The overall gain of the amplifier is 75 dB. By ing a power mixing network, the earth station can simultaneously transmit an FDM/FM carrier and an SCPC carrier to the same transponder.

Low-Noise Amplifier. Low-noise amplification is accomplished by a thermo-electrically cooled 55K FET amplifier. This amplifier has good performance in terms of gain-frequency response and gain stability.

SCPC Up/Down Frequency Converter. The up/down frequency conversion is accomplished by a two-stage conversion process; the intermediate-frequency (I.F.) is 70 MHz±18 MHz, the radio-frequency (RF) for the up/down converters is respectively 5925-6425 MHz and 3700-4200 MHz. The instantaneous operating bandwidth is 36 MHz. This is the first time that the SCPC up/down frequency converters have been used in the 64 kb/s data circuit; it has sufficiently low phase noise to meet the performance requirements for data transmission.

SCPC Terminal Equipment. The SCPC terminal uses equipment also developed by this institute; this equipment is technologically mature and has been widely applied in domestic satellite communications systems. Equipment includes the CVSD codec [coder/decoder chip], the signaling system, the differential coder, the BPSK [binary phase shift keying] modem, and the transceiver channel frequency synthesizer. The telephone channels (including audio-frequency telegraphy, single-channel facsimile, and inband data transmission at 1200 b/s and 2400 b/s) and the ground circuits use 4-line audio-frequency interfaces. The 56 kb/s data channels are composed of the following components: the data interface, the R7/8 error-correcting codec, the QPSK [quarternary phase-shift keying] modem, and the transceiver frequency synthesizer.

FDM/FM Equipment. FDM/FM equipment has had a long history in satellite communications and is still in wide use today. The size of the equipment has undergone miniaturization, and an entire series of FDM/FM equipment (24-972 lines) has been developed. The equipment has a "card" shaped structure, and the entire system, which consists of the up/down frequency converters, the modem, the I.F. filter, the baseband processing unit and the monitoring circuit, fits in a 19-inch box.

Monitoring and Control (MAC) Equipment. Each subsystem of the earth station can perform its own monitoring and control function, but the system also has a microprocessor-controlled MAC subsystem which can perform the following real-time control functions:

automatic control and tracking of the antenna,

remote-control operation of the high-power amplifier,

remote-control switching of the backup high-power amplifier, and

remote-control switching of the backup low-noise amplifier.

The MAC subsystem uses the new MAC software which has been developed for an IBM-PC microcomputer. The software is designed to extend the functions of the peripheral equipment, which include:

display of the functional block diagram of the earth station system and its subsystems,

display of data at the equipment monitoring points,

display of equipment faults (status and data display), and

real-time print-out of equipment status.

2. System Reliability

For a variety of different reasons, the component reliability of Chinese-built equipment is less than satisfactory. However, by paying attention to the availability issue in system design and system configuration, a high availability index can still be achieved in an earth station with all-Chinese-made equipment. The calculated availability indices for the 11-m-antenna earth station are presented in Table 1. It has been shown from analysis that the overall availability of this Chinese-built earth station exceeds 99.9%, and its maintainability index is much higher than that of imported equipment.

Table 1

	MTBF(hr)	Availability
Antenna system	1.3×10^3	0.999725
Uplink	6.030×10^3	0.999865
Downlink	1.3×10^4	0.999923
Power-supply system	2×10^4	0.999900
Total	3.3×10^3	0.999410

3. Test Results

In April 1989, as part of the certification process, MPT conducted full-scale tests of the system parameters and examined the operational performance of the system. The test results showed that all technical indices meet design requirements, and its operational performance is superior to that of existing earth stations. The results of certification (key indices) are summarized as follows:

	Requirement	Test Result
Earth station G/T	$\geqslant 31.2$ dB/K	31.7 db/K
RF stray output	$\leqslant 4$ dBW/4kHz	-11.3 dBW/4kHz (972-ch. FDM/FM)
Sidelobe characteristics		Meets CCIR specifications
S/N and C/N test	(for C/N=17.8 dB, S/N $\geqslant$ 50 dB;for C/N=12.8 dB, S/N $\geqslant$ 43 dB)	See Table 2
SCPC data BER test	See Table 3	See Table 3

36

Table 2 (972-channel FDM/FM)

| | Test-channel frequency (kHz) | | | | |
C/N (dB)	16	98	240	1248	3886
17.8	60/64.5	61/64	61/64	56/58.5	53/57.5
15.8	59.5/63	60.5/63	60.5/63	55.5/57	52.5/54
13.8	58.5/60.5	59.5/61.5	59/61.5	54/55.5	51/52
12.8	57/60	57.5/59.5	57/59	52/53	49/49.5
11.8	57/59	58/59	57.5/59	52.5/51	49/49.5
9.8	56/57.5	56/57	56/57	50.5/51	47.5/48
7.8	54.5/55.5	54.5/55	54.5/55	48.5/49	45.5/45.5
5.8	50.5/54	50.5/53.5	50.5/53.5	45.5/46.5	43/43.5
High C/N	61.5/68.5	64/74.5	64/76.5	60/77.5	57.5/77.5

Example: 60/64.5 = signal-to-system-noise ratio (dB)/signal-to-base-noise ratio (dB)

37

Table 3

Signal channel	Channel state	BER requirement	Freq. channel	Test results			Neighboring frequency channel	
				1st test	2nd test	3rd test		
1	A	$C/N=15.5dB$ $P_e \leqslant 1\times10^{-6}$	798	6×10^{-7}	6×10^{-7}		797	799
			002	$<1\times10^{-7}$	$<1\times10^{-7}$		001	003
			403	1.5×10^{-6}	1×10^{-6}	9×10^{-7}	402	404
1	A	$C/N=13.5dB$ $P_e \leqslant 1\times10^{-4}$ (or 3360/10 min.)	403	1×10^{-6}	4×10^{-6}	2×10^{-6}	402	404
			510	5×10^{-6}	2×10^{-6}	4×10^{-6}	509	511
			510	66			509	511
1	C	$C/N=13.5dB$ $P_e \leqslant 1\times10^{-7}$	403	$<1\times10^{-7}$	$<1\times10^{-7}$		402	404
			002	$<1\times10^{-7}$	$<1\times10^{-7}$		001	003
			798	$<1\times10^{-7}$	$<1\times10^{-7}$		797	799

A state: no FEC, no scramble code.   C state: with FEC and scramble code.
Only the test results of the FDM/FM 972-channel and the SCPC data channels are presented here; the other test results are not shown.

4. Conclusion

The results of certification tests and operational tests by MPT have shown that the technical performance indices of the 11-m-antenna earth station meet all design requirements. The earth station is ready for large-scale production and can be used as a type II station in the existing satellite communications network.

- END -

END OF
FICHE
DATE FILMED

~ July 1990